

Supporting Information

Sorption and Transport of Vapors in ZIF-11: Adsorption, Diffusion, and Linker Flexibility

*Brian R. Pimentel^{a†}, Melinda L. Jue^{ab†}, Er-Kang Zhou^a, Ross J. Verploegh^a, Johannes Leisen^c,
David S. Sholl^a, Ryan P. Lively^{a*}*

^aSchool of Chemical & Biomolecular Engineering, 311 Ferst Drive, Georgia Institute of
Technology, Atlanta, Georgia 30332, United States

^bCurrent address: Physical and Life Sciences, 7000 East Avenue, Lawrence Livermore National
Laboratory, Livermore, California 94550, United States

^cSchool of Chemistry and Biochemistry, 901 Atlantic Drive, Georgia Institute of Technology,
Atlanta, Georgia 30332, United States

Table of Contents

S1. Material Characterization.....	S3
S2. Calculation of Sorbate Diffusivities in ZIF-11.....	S5
S3. Thermodynamic Correction to Diffusion.....	S14
S4. IAST Selectivity Calculations.....	S15
S5. Determination of Linker Librational Amplitude from Solid Echo Experiments.....	S17
S6. Tabular Data.....	S23
S7. References.....	S34

S1. Material Characterization

Powder XRD of the samples indicates crystalline materials with good agreement to the simulated patterns (**Figure S1**). SEM images were analyzed using the ImageJ software package to determine the crystal size distribution for the non-deuterated ZIF-11 samples. These revealed crystals with sharp facets of similar morphology with little twinning or crystal agglomeration that could interfere with diffusion measurements (**Figure S2**). Samples were referred to by their average crystal diameter: $36\ \mu\text{m} \pm 6$ and $22\ \mu\text{m} \pm 2$.

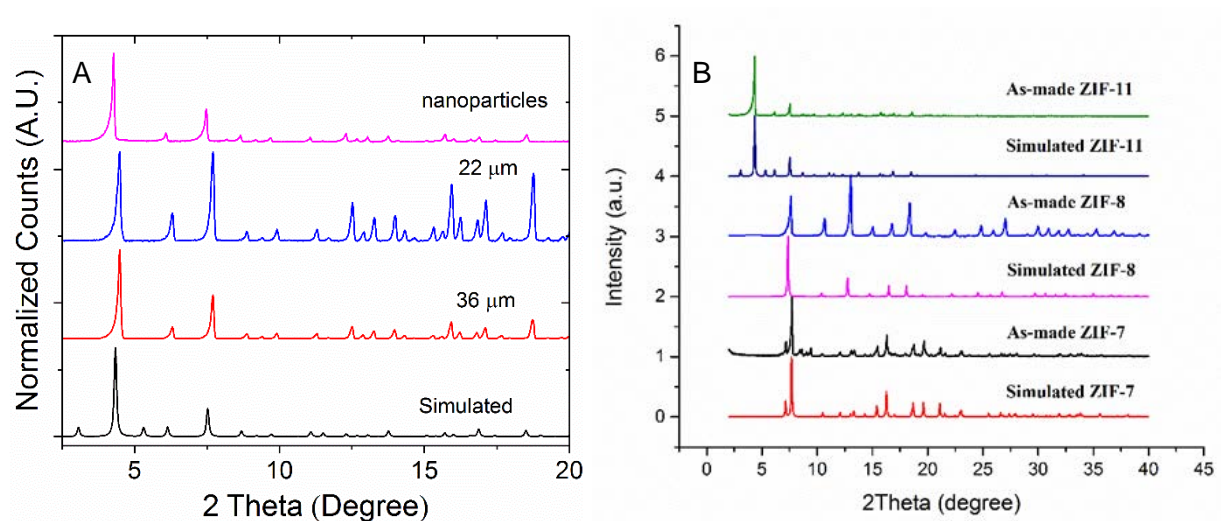


Figure S1. A) Powder XRD patterns of ZIF-11 samples used for sorption experiments and B) d-ZIF samples used for solid state NMR experiments compared to their simulated structure patterns.

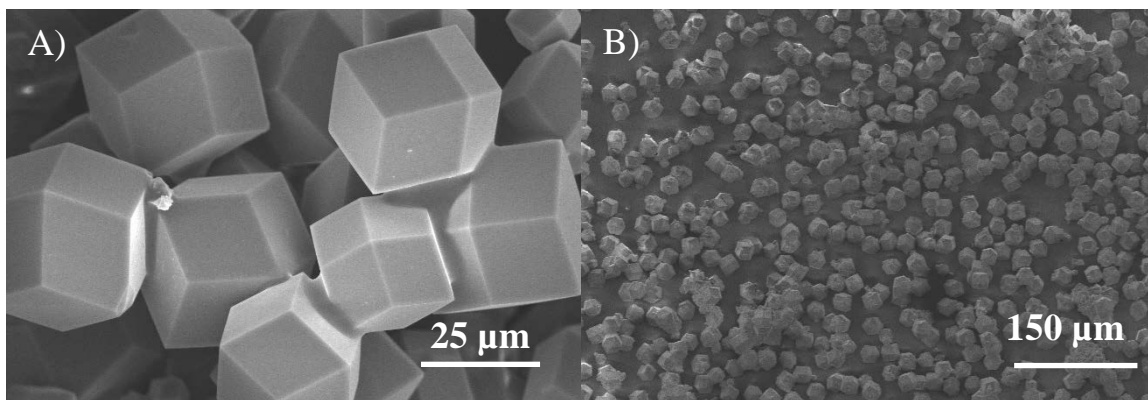


Figure S2. A) SEM images of 36 μm ZIF-11 and B) 22 μm ZIF-11 samples used for diffusion experiments.

S2. Calculation of Sorbate Diffusivities in ZIF-11

Accurate determination of diffusivity is a critical step in microporous material characterization, as the species' diffusivity controls the mass transfer in sorbent applications and contributes significantly to the productivity in membrane applications. Furthermore, the ratio of sorption and diffusion values between two species dictates the overall selectivity in any given permeation-type application, with large errors in measurements possibly leading to erroneous process designs.

The determination of equilibrium isotherms for both gas and vapor systems is well established and readily available via commercial instruments and software packages using either gravimetric or volumetric techniques. However, the analysis of transient uptake data is much more nuanced and not routine, and therefore is generally not included in the analysis software of most sorption equipment.

Typically, the measured transient uptake is normalized and fit to the analytical solution of the diffusion problem using appropriate geometric coordinates and boundary conditions. In all cases, the value of the diffusivity parameter is fit, and other parameters may be estimated with varying degrees of certainty, or be fit parameters themselves. The most commonly applied boundary condition to the diffusion problem is the instantaneous step-change in surface concentration $C = C_1$ at $t > 0$ and $R = a$, with an initial condition of $C = C_0$ at $t = 0$ at all points. In a sphere of radius a , this yields (S1) where M_t is the mass at time t , M_∞ is the equilibrium mass, and D is the diffusion coefficient.¹

$$\frac{M_t}{M_\infty} = 1 - \frac{6}{\pi^2} \sum_{n=1}^{\infty} \frac{1}{n^2} \exp\left(-\frac{Dn^2\pi^2 t}{a^2}\right) \quad (\text{S1})$$

This is generally appropriate in gravimetric systems of large volumes where the sorbent is dosed rapidly without the use of a carrier gas or in any other system where the concentration change can be said to be nearly instantaneous and the depletion of the sorbate in the chamber is negligible. In nearly all volumetric systems, depletion of the sorbate in the chamber is necessarily significant and therefore should be modeled using as diffusion from a well-stirred solution of limited volume, (S2).¹

$$\frac{M_t}{M_\infty} = 1 - \sum_{n=1}^{\infty} \frac{6\alpha(\alpha + 1) \exp\left(-\frac{Dq_n^2 t}{a^2}\right)}{9 + 9\alpha + q_n^2 \alpha^2} \quad (\text{S2})$$

where q_n are the non-zero roots of (S3)

$$\tan(q_n) = \frac{3q_n}{3 + \alpha q_n^2} \quad (\text{S3})$$

and α is related to the final fractional uptake of the solute by (S4) where V is the volume of the chamber excluding the sorbent.¹

$$\frac{M_\infty}{VC_0} = \frac{1}{1 + \alpha} \quad (\text{S4})$$

This model is used to evaluate the diffusion of gaseous sorbates in this work (e.g., propane and *n*-butane).

There exists other experimental apparatuses commonly employed in the gathering of diffusion data in which the change in concentration is achieved by a change in gas flow composition to the sample chamber. Here, we typically refer to gravimetric units, where the sample chamber represents a reasonably sized volume relative to the inlet gas flow and not methods such as Zero Length Columns (ZLC). Two examples of such are (1) Thermal Gravimetric Analysis (TGA) units,

where a change in gas flow from pure N₂ to a pre-mixed 10% CO₂ in N₂ could be used to analyze CO₂ diffusion under flue gas conditions, and (2) saturated vapor flow units—such as the VTI-SA+ unit employed in this study—where mass flow controllers combine a dry and saturated vapor stream to achieve the desired relative saturation within the sample chamber. In both these units, the flow of gas into the sample chamber is not perfect plug flow, which would result in an instantaneous surface concentration change, ignoring external transport barriers. It is more accurately modeled as a continuously stirred tank (CST), where the change in concentration C within the chamber (and the surface) is approximated by an exponential approach to the inlet concentration C_0 as given by (S5)

$$C(t) = C_0 \left[1 - \exp\left(-\frac{t}{\tau}\right) \right] \quad (\text{S5})$$

where $\tau = V/\dot{V}$, the ratio of the chamber volume V to the feed volumetric flowrate \dot{V} (note, in *The Mathematics of Diffusion*, $\beta = 1/\tau$).¹ This boundary condition results in a very different analytical solution to the diffusion equation, (S6).

$$\begin{aligned} \frac{M_t}{M_\infty} = & 1 - \frac{3D\tau}{a^2} \exp\left(-\frac{t}{\tau}\right) \left\{ 1 - \left(\frac{a^2}{D\tau}\right)^{\frac{1}{2}} \cot\left(\left(\frac{a^2}{D\tau}\right)^{\frac{1}{2}}\right) \right\} \\ & + \frac{6a^2}{\pi^2 D\tau} \sum_{n=1}^{\infty} \frac{\exp(-(Dn^2 \pi^2 t)/a^2)}{n^2(n^2 \pi^2 - a^2/D\tau)} \end{aligned} \quad (\text{S6})$$

This variable surface concentration boundary condition leads to an uptake curve that appears sigmoidal, rather than linear, at short time scales when normalized mass uptake is plotted against $t^{\frac{1}{2}}$. Otherwise, sigmoidal behavior is generally indicative of surface barriers to diffusion or other external transport limitations. To demonstrate the lack of step change profile within the VTI-

SA+ sample chamber, the vapor composition at the outlet of the sample chamber was monitored via mass spectroscopy over a complete isotherm measurement experiment. Isotherms were measured in triplicate (denoted as a sequence) using an empty sample pan. Both ethanol and *n*-hexane vapors were investigated to determine any τ dependence on the choice of sorbate. The initial stream equilibration bypass used in the system was disabled for these experiments, but analysis of the mass spectroscopy data indicates that the mass flow controllers in the system are able to reach the desired set point within a matter of seconds.

Characteristic plots of the normalized outlet concentration over time are presented in **Figure S3**, where it is clear that the concentration change within the sample chamber follows more closely an exponential function rather than an instantaneous step change. In general, the first step of the sequence (not of each isotherm) was found to have a noticeably longer time constant independent of vapor choice. In general, ethanol exhibited a shorter τ than *n*-hexane, although both displayed a good deal of variation. There appears to be no thermodynamic explanation for this discrepancy in behavior. Furthermore, there is no obvious trend between τ and the relative saturation, which would relate to the mass flow controller set points. We therefore used the average τ collected from both vapors (107 s) and the associated standard error (36 s) in our subsequent diffusion analysis.

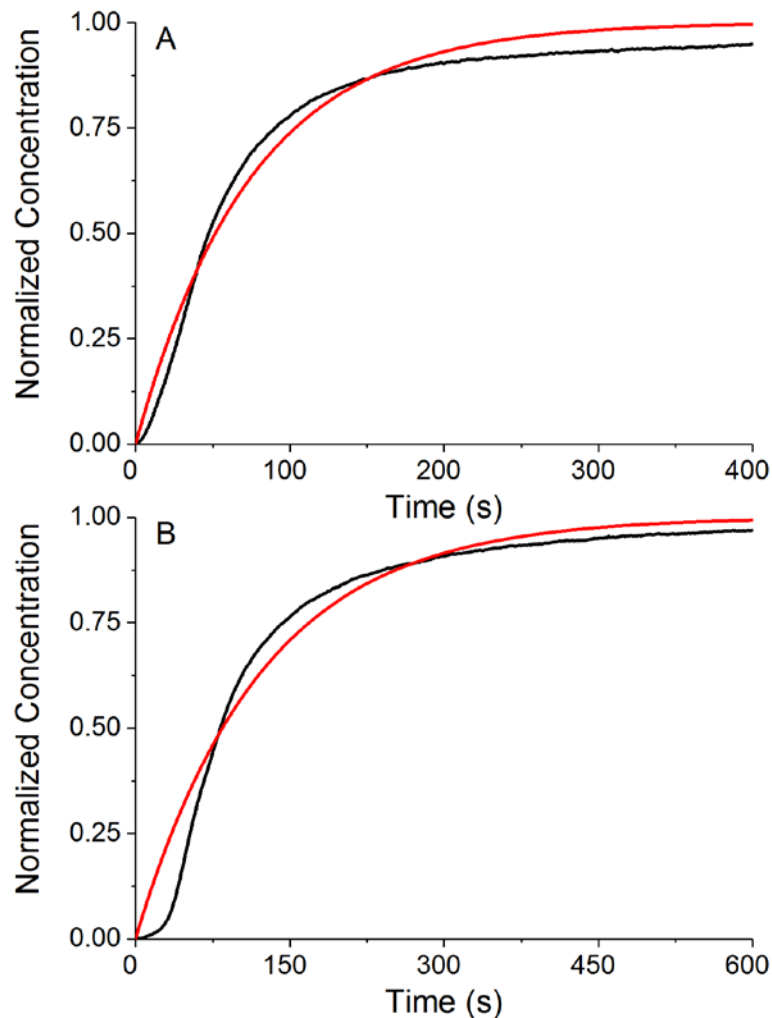


Figure S3. A) Normalized VTI-SA+ outlet concentration of ethanol and B) *n*-hexane after a set-point change. The black curve indicates the normalized mass spectrometer data with the exponential curve fit overlaid in red.

In a similar manner to which volumetric adsorption kinetics may be affected by the speed of the valve opening in a pressure decay system,² the time constant of the concentration change may severely limit the ability to estimate diffusivity in a flowing gravimetric system if the diffusion phenomena is sufficiently fast. The ratio of the diffusive and the external time constants can be described as $\phi = a^2/D\tau$. A plot of the analytical solutions with varying ϕ values is shown in

Figure S4.¹ As ϕ decreases, the uptake is increasingly dominated by the boundary condition rather than diffusion.

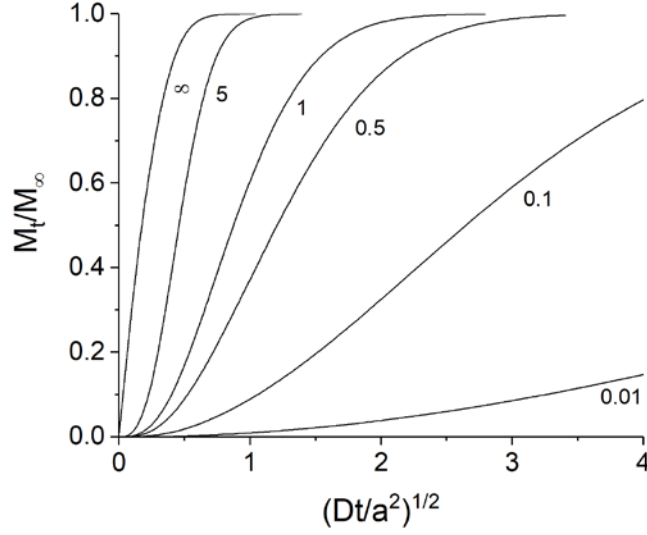


Figure S4. Analytical solutions to the diffusion equation with an exponential boundary condition for different ϕ .

With decreasing ϕ , the analytical solution becomes less sensitive to the value of the diffusivity constant and introduces increasing margins of error in the data fitting. To demonstrate this principle, we estimate the associated error in diffusivity assuming a 2.5% standard deviation in the reproducibility of the data at 50% uptake. This measure of reproducibility error is an estimate based on our own data. The resulting error in diffusivity σ_D can be estimated by a combination of variances assuming uncorrelated variables (S7), where σ_M is the error associated with the mass and σ_τ is the error associated with the time constant.

$$\sigma_D^2 = \sigma_M^2 \left(\frac{\partial D}{\partial M} \right)^2 + \sigma_\tau^2 \left(\frac{\partial D}{\partial \tau} \right)^2 \quad (\text{S7})$$

Given the complex nature of the equation, $\partial D/\partial x_i$ were estimated by applying the derivative function to the analytical solution of the uptake in Wolfram Mathematica rather than solved analytically. **Figure S5** demonstrates the increasing error associated with the estimation of the diffusivity parameter as ϕ decreases.

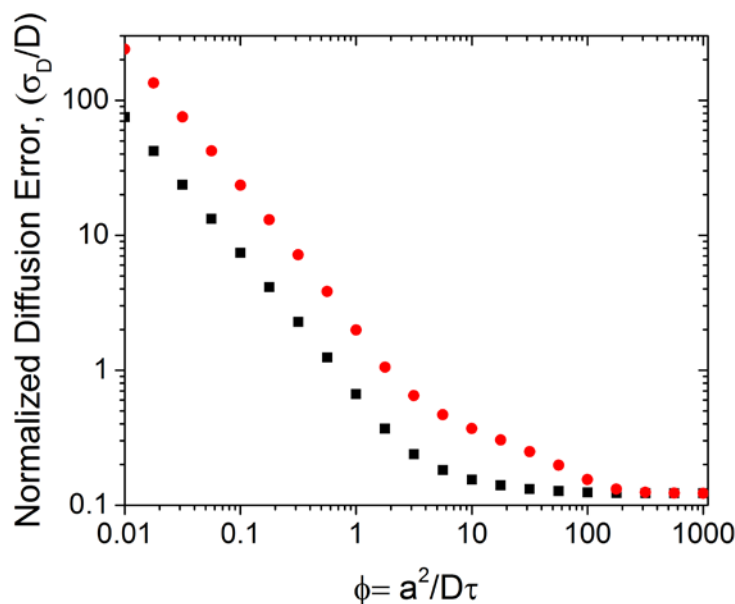


Figure S5. Estimated error in the fitted diffusivity as a function of ϕ in the case of an exponential boundary condition. The fit errors are for using a known time constant (black squares) and for the error associated with the measured τ variability (red circles).

In the case of a known τ , the relative error in the fit begins to rise noticeably at values of $\phi < 10$ and becomes significant at $\phi < 1$. Incorporating the uncertainty in the τ measurements yields noticeably increased error in the diffusion fits at $\phi < 100$ over the known τ case. This analysis should serve as an “upper limit” for the measurable diffusivity values obtained from each instrument, where ϕ should likely be kept above 10 to minimize the role of external control on fit sensitivity. For the fastest diffusing vapors in this work (i.e., methanol), ϕ typically exceeded 30,

although some of the higher diffusion values of *n*-hexane had ϕ values as low as 5. Other significant sources of error in the data collection (such as sampling rate) and in the fitting (such as goodness of fit) are omitted from this analysis for simplicity. **Table S1** shows the differences in fitted ethanol diffusivity values for data fitting using a fixed τ versus a multivariate fit that allows for a variable τ . Generally, the errors are within an order of magnitude, although we discovered that some uptake values showed τ values well above the measured average. These high values were necessary to produce a reasonable fit to the experimental data, even though they did not necessarily affect the fitted diffusivity value. Therefore, significant unexplained variation in the time constant across solvents and relative saturation steps may exist. Eliminating these errors could further reduce the relative fitting error for the time constant.

Table S1. Calculated thermodynamically corrected diffusivities of ethanol in 36 μm ZIF-11 at 308 K with a 1-parameter fit (D_1) and a 2-parameter fit (D_2). τ_1 has a value of 107 s, as previously described. τ_2 is the fitted τ value for that experiment.

	Relative Saturation					
	0.025	0.05	0.1	0.15	0.2	0.3
D_1/D_2	0.62	1.13	0.69	1.07	0.91	0.3
τ_2	180	79	374	99	119	122

It is also important to ensure that the two different crystal sizes used in this investigation exhibit similar diffusive behavior. To this end, 1-propanol diffusion at infinite dilution was analyzed in both ZIF-11 samples. **Table S2** shows the fitted diffusivity values using both a fixed τ_1 of 107 s and a variable τ_2 ; the values are within an order of magnitude, lending confidence to the direct comparison of transport properties between the two ZIF-11 samples.

Table S2. 1-Propanol diffusivity in different crystal sizes of ZIF-11 at 308 K at infinite dilution

Crystal Size (μm)	Diffusion Coefficient (cm^2/s)	
	τ_1^{a}	τ_2^{b}
22	5.0×10^{-11}	1.1×10^{-10} (325)
36	3.0×10^{-11}	9.1×10^{-11} (1245)

^a τ_1 is fixed at 107 s.

^b τ_2 is a fitted parameter and shown in parenthesis.

Furthermore, it is also important to verify that the size distribution of the crystals is sufficiently narrow to allow for a single average value to be used for the diffusion calculations. The diffusion coefficients for the fastest (methanol and 1-propanol for the 36 and 22 μm crystals, respectively) and slowest (*n*-heptane) sorbates used were re-calculated using the weighted distribution fit from a five-bin histogram of the crystal population. The diffusion coefficients determined using the single and weighted fits are shown in **Table S3**.

Table S3. Comparison of sorbate diffusion coefficients calculated using the number average radius and the weight average from the population distribution.

Sorbate	Diffusivity with Average Radius (cm^2/s)	Diffusivity with Weighted Fit Distribution (cm^2/s)
Methanol	7.8×10^{-10}	4.2×10^{-10}
1-Propanol	5.0×10^{-11}	5.6×10^{-11}
<i>n</i> -Heptane	2.25×10^{-11}	2.64×10^{-11}

Based on this analysis, the error introduced to the diffusion estimations by the use of a single average crystal size is relatively minor and falls within the experimental accuracy of the measurements themselves.

S3. Thermodynamic Correction to Diffusion

Observed diffusivities, that is, the results of fitting operations, are reported as transport diffusivities D_T . This is indicative of the observed diffusion rate determined from the analytical solutions. These values are dependent on the sorption behavior—as expressed by the shape of the sorption isotherm—and are often corrected to eliminate this effect. (S8) shows the Darken correction factor that relates the thermodynamically corrected diffusion coefficient \mathfrak{D} to the transport diffusion coefficient by the pressure p and concentration C during diffusion.³

$$D_T = \mathfrak{D} \frac{d \ln(p)}{d \ln(C)} \quad (\text{S8})$$

In the case of non-differential pressure steps, \mathfrak{D} is corrected by the average value of the factor over the adsorbed range, which takes the following form for Langmuir isotherms (S9).⁴

$$\begin{aligned} \frac{D_T}{\mathfrak{D}} = \frac{5}{U_\infty^5 - U_0^5} & \left[\frac{1}{6} \ln \left[\frac{1 + U_\infty + U_\infty^2}{(1 - U_\infty)^2} \frac{(1 - U_0)^2}{1 + U_0 + U_0^2} \right] \right. \\ & \left. - \frac{1}{\sqrt{3}} \tan^{-1} \left(1 + \frac{2U_\infty}{\sqrt{3}} \right) + \frac{1}{\sqrt{3}} \tan^{-1} \left(\frac{1 + 2U_0}{\sqrt{3}} \right) + \frac{U_0^2 - U_\infty^2}{2} \right] \end{aligned} \quad (\text{S9})$$

$U_0 = \theta_0^{1/3}$, $U_\infty = \theta_\infty^{1/3}$, θ_0 is the initial surface coverage of the sorbent, and θ_∞ is the final surface coverage. In this work, all gas \mathfrak{D} values were corrected using (S9) given their good Langmuir fit, while vapor diffusivities were corrected using the Darken factor in (S8).

S4. IAST Selectivity Calculations

IAST selectivities were calculated for adsorption from the gas phase in equilibrium with a given water/alcohol composition. Gas phase compositions were calculated using the UNIF-LL activity model in Aspen Plus for mixtures of water and C₁-C₄ alcohols at 308 K. A linear interpolation of the water and alcohol isotherms were used according to the following algorithm.⁵

The initial reduced spreading pressure z was estimated by (S10).

$$z = \frac{\pi A}{R_g T} = \sum_{j=1}^n y_j \int_0^P \frac{C_{\mu j}}{P_j} dP_j \quad (\text{S10})$$

Where y_j is the vapor mole fraction, P_j the partial pressure, and $C_{\mu j}$ the adsorbed concentration of component j of n species. The hypothetical pressure of each component (P_j^0) equivalent to the spreading pressure (S11) was iterated using a Newton-Raphson method until convergence, with the actual partial pressures as initial guesses.

$$P_j^{0(k+1)} = P_j^{0(k)} - \frac{G(P_j^{0(k)})}{G'(P_j^{0(k)})} \quad (\text{S11})$$

Where

$$G = \int_0^{P_j^0} \frac{C_{\mu j}}{P_j} dP_j - z \quad (\text{S12})$$

and

$$G' = \frac{C_{\mu j}^0}{P_j^0} \quad (\text{S13})$$

The new spreading pressure was recalculated using the new hypothetical pressures, again with a Newton-Raphson method until convergence (**S14**).

$$z^{k+1} = z^k - \frac{F}{F'} \quad (\text{S14})$$

Where

$$F(z^k) = \sum_{j=1}^n \frac{Py_j}{P_j^0} - 1 \quad (\text{S15})$$

and

$$F'(z^k) = - \sum_{j=1}^n \frac{Py_j}{P_j^0 C_{\mu j}^0} \quad (\text{S16})$$

The total adsorbed quantity ($C_{\mu T}$) is given by (**S17**).

$$\frac{1}{C_{\mu T}} = \sum \frac{x}{C_{\mu}^0} \quad (\text{S17})$$

Where the adsorbed mole fraction (x_j) is defined as

$$x_j = \frac{Py_j}{P_j^0} \quad (\text{S18})$$

S5. Determination of Linker Librational Amplitude from Solid Echo Experiments

^2H solid-state NMR is a well-established, powerful method to investigate the geometry of molecular motions in solids.⁶ ^2H solid-state NMR spectra are dominated by the quadrupolar energy terms experienced by the ^2H nucleus in a magnetic field. In most cases, the relevant quadrupolar tensor can be considered to be axially symmetric and its axis is aligned with a C- ^2H bond. If no molecular motion takes place, the angle θ of this tensor/bond with respect to the magnetic field determines the corresponding frequencies ω in the NMR spectrum according to (S19) where ω_0 is the Larmor frequency and δ_Q is the quadrupolar coupling constant.

$$\omega = \omega_0 \pm \frac{1}{2} \delta_Q (3 \cos^2 \theta - 1) \quad (\text{S19})$$

Molecular motions are associated with a reorientation of the tensor with respect to the magnetic field. If they occur with a rate which is significantly larger than the frequency value δ_Q , averaged frequencies will be detected according to (S20).

$$\omega = \omega_0 \pm \frac{1}{2} \delta_Q \langle 3 \cos^2 \theta - 1 \rangle_\theta \quad (\text{S20})$$

Random distribution of rigid samples are associated with a spherical distribution of the angle θ leading to the characteristic Pake pattern according to (S19). Molecular motion leads to line narrowing and changes in this lineshape according to (S20). Hence, (S20) allows for the modeling of ^2H lineshapes with suitable models of molecular motion. In our case, we used the software package NMR WEBLAB 6.3.3,⁷ which conveniently allows the interactive online modeling of ^2H NMR spectra.

Figure S6 shows some of the ^2H NMR spectra of d-ZIF-7, -8, and -11 recorded over a range of more than 100 K. On one hand, very similar spectra were found for d-ZIF-11 and d-ZIF-7 consisting of a Pake pattern with a quadrupolar splitting (i.e. the frequency width defined by the singularities of the Pake pattern) ranging between 128 and 130 kHz. On the other hand, the spectrum of d-ZIF-8 exhibits an additional Pake pattern due to the "motionally-averaged" motion of the rotating methyl group, where the quadrupolar splitting is in the range of 35-37 kHz. In all cases, changes in temperature did not result in significant changes to the lineshape, only small reductions of the quadrupolar splitting with increasing temperatures.

In order to quantify the observed spectra, a simple model was used to relate the measured splittings to the molecular motions. For both the benzimidazole-4,5,6,7- d_4 used in d-ZIF-7 and d-ZIF-11 and the 2-methylimidazole- d_6 used in d-ZIF-8, the axis defined by the two nitrogen atoms was considered to be fixed in space. The motion of the linkers was assumed to be a “saloon door” type motion, i.e., the motion is described by a forward-backward rotation (libration) of the rotational axis with amplitude of $\Delta\phi$ (**Figure S7**) around a preferred position.

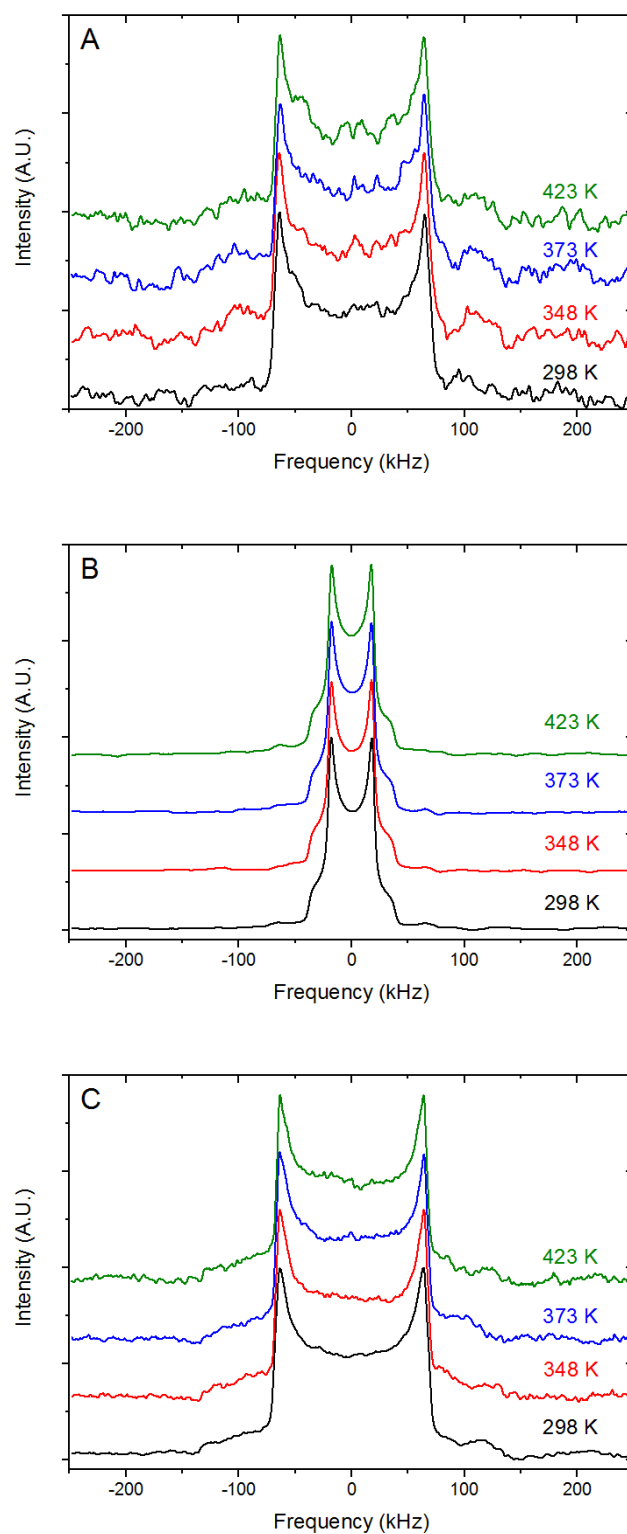


Figure S6. Pake patterns of A) d-ZIF-7 B) d-ZIF-8, and C) d-ZIF-11 measured between 298 and 423 K.

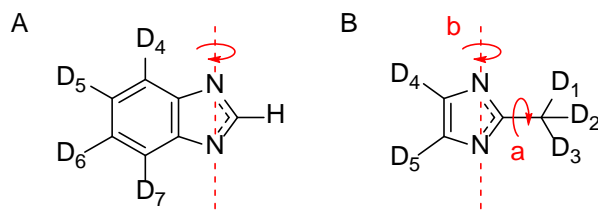


Figure S7. A) The principal axis of rotation for benzimidazole-4,5,6,7-d₄ used in d-ZIF-7 and d-ZIF-11. B) The two axes of rotation for 2-methylimidazole-d₆ used in d-ZIF-8.

We are well aware that the above model provides a simplification and that motion of the principal axis defined by the two nitrogen atoms is likely to exist. A more complex motional model involving conformational exchanges in ZIFs has been proposed by Jobic;⁸ however, this model also has its limitations: a mere exchange between two conformers will not account for the experimentally observed continuous change in the quadrupolar splitting with temperature. We are also aware that for the case of rotation around the cone angle of 0° (positions 4 and 7 for benzimidazole-4,5,6,7-d₄), any motions around the principal axis will not change θ and therefore, will not affect the resulting spectrum. This does not apply for the ²H in the 5 and 6 positions, which create a cone angle of 60°. Hence, for d-ZIF-7 and d-ZIF-11 containing benzimidazole-4,5,6,7-d₄, the experimental spectrum must be an overlay of two cone angles. Our simulations have shown that at small to moderate librational angles, this overlay is not immediately obvious and the spectrum corresponding to the 5 and 6 positions will lead to an apparent reduction of the quadrupolar splitting. Hence, we used positions 5 and 6 to calculate the quadrupolar splittings for d-ZIF-7 and d-ZIF-11.

Measured quadrupolar splittings together with the librational amplitudes for both molecules assuming a quadrupolar coupling constant of $\delta_Q = 135 \text{ kHz}$ are shown in **Figure S8**.

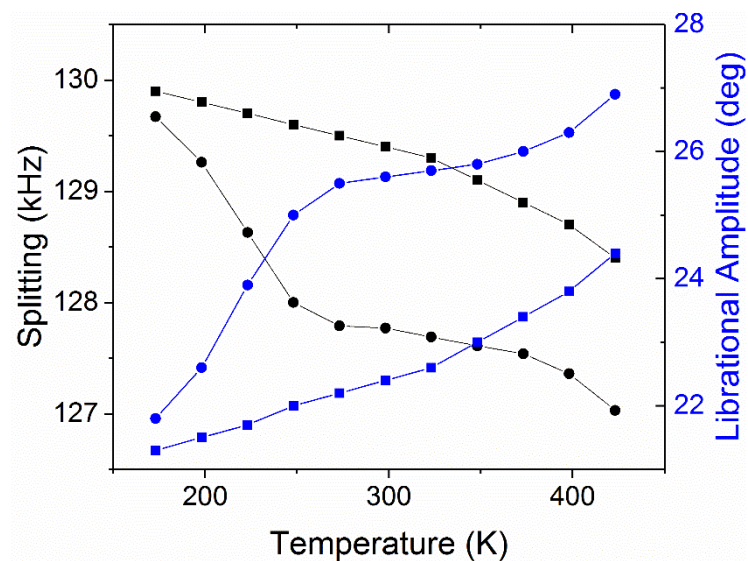


Figure S8. Quadrupolar splitting (blue) and librational amplitude (black) of d-ZIF-7 (squares) and d-ZIF-11 (circles) measured from 173 to 423 K.

Similar to benzimidazole-4,5,6,7- d_4 , the 2-methylimidazole- d_6 in d-ZIF-8 requires overlaying spectra that can be described by a quadrupolar coupling constant of $\delta_Q = 135 \text{ kHz}$ for the 4 and 5 position (cone angle 72°) and $\delta_Q = 42.6 \text{ kHz}$ for the average tensor formed by the rotating methyl group (cone angle 90°). Simulations of the 1-3 positions resulted in librational amplitudes on the order of $38\text{--}43^\circ$. However, due to a limited signal to noise ratio, it was not possible to accurately determine experimental quadrupolar splittings for positions 4 and 5 (c.f. **Figure S7B**) and to reliably determine the corresponding librational amplitude.

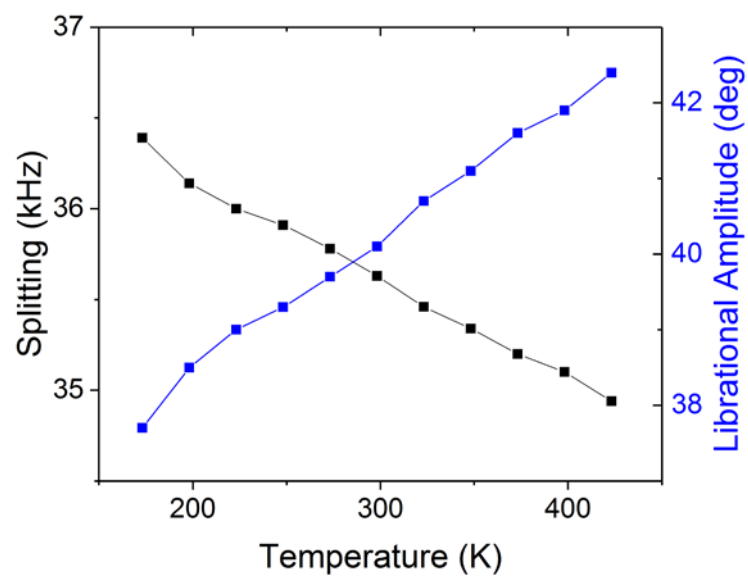


Figure S9. Quadrupolar splitting and librational amplitude of d-ZIF-8 measured from 173 to 423

K

S6. Tabular Data

Table S4. Adsorption isotherms of alcohol and water vapors in ZIF-11 (Figure 1A) at 308 K

Sorbate	Relative Pressure (P/P ₀)	Uptake (mmol/g)	Standard Deviation (mmol/g)
Methanol	0.05	0.547	0.019
	0.1	1.967	0.228
	0.125	4.043	0.118
	0.15	5.794	0.122
	0.2	6.764	0.023
	0.25	7.148	0.023
	0.3	7.404	0.011
	0.4	7.740	0.011
	0.5	7.974	0.010
	0.6	8.141	0.007
	0.7	8.274	0.008
	0.8	8.373	0.018
Ethanol	0.025	0.595	0.004
	0.05	0.950	0.007
	0.1	4.062	0.097
	0.15	4.582	0.014
	0.2	4.872	0.012
	0.3	5.192	0.016
	0.4	5.394	0.014
	0.5	5.535	0.016
	0.6	5.648	0.017
	0.7	5.741	0.018
	0.8	5.808	0.014
1-Propanol	0.01	0.564	0.011
	0.02	0.704	0.008
	0.03	1.730	0.111
	0.04	2.355	0.032
	0.05	2.738	0.029
	0.07	3.045	0.020
	0.10	3.196	0.018
	0.20	3.523	0.016
	0.30	3.721	0.014

	0.40	3.977	0.012
	0.50	4.058	0.015
	0.60	4.116	0.014
	0.70	4.153	0.016
	0.80	4.178	0.020
1-Butanol	0.02	2.305	0.010
	0.025	2.375	0.033
	0.05	2.578	0.032
	0.075	2.684	0.032
	0.1	2.760	0.032
	0.2	2.955	0.031
	0.3	3.067	0.032
	0.4	3.154	0.033
	0.5	3.210	0.034
	0.6	3.255	0.034
	0.7	3.301	0.040
	0.8	3.333	0.039
Water	0.05	0.004	0.010
	0.10	0.006	0.012
	0.20	0.011	0.011
	0.30	0.015	0.010
	0.40	0.020	0.011
	0.50	0.027	0.012
	0.60	0.035	0.016
	0.70	0.043	0.018
	0.80	0.051	0.017
	0.90	0.169	0.026
	0.95	0.386	0.072
	0.99	0.611	0.150

Table S5. IAST Selectivities of alcohol vs. water in ZIF-11 (Figure 1B) at 308 K

Sorbate	Liquid Alcohol Fraction (-)	Selectivity (ROH/H ₂ O)
Methanol	0.003	6.9
	0.007	5.0
	0.010	4.3
	0.013	3.8
	0.017	3.6
	0.020	3.4
	0.023	3.2
	0.027	3.1
	0.030	3.1
	0.033	3.0
	0.037	3.0
	0.040	2.9
	0.043	2.9
	0.047	2.9
	0.050	2.9
Ethanol	0.003	38.2
	0.007	34.6
	0.010	34.5
	0.013	36.5
	0.017	38.7
	0.020	40.6
	0.023	41.6
	0.027	42.0
	0.030	42.1
	0.033	42.0
	0.037	41.8
	0.040	41.5
	0.043	41.2
	0.047	40.8
	0.050	40.5
1-Propanol	0.003	37.1
	0.007	26.4
	0.010	21.4
	0.013	18.5
	0.017	16.6

	0.020	15.2
	0.023	14.2
	0.027	13.4
	0.030	12.8
	0.033	12.3
	0.037	11.9
	0.040	11.6
	0.043	11.3
	0.047	11.1
	0.050	10.8
1-Butanol	0.003	54.4
	0.007	34.5
	0.010	27.0
	0.013	23.1
	0.017	20.7
	0.020	19.2

Table S6. Adsorption isotherms of hydrocarbon vapors in ZIF-11 at 308 K (Figure 2A)

Sorbate	Relative Pressure (P/P ₀)	Uptake (mmol/g)	Standard Deviation (mmol/g)
Hexane	0.01	1.757	0.003
	0.02	1.812	0.005
	0.02	1.856	0.006
	0.03	1.890	0.006
	0.05	1.995	0.007
	0.08	2.058	0.005
	0.10	2.106	0.006
	0.20	2.214	0.004
	0.30	2.270	0.003
	0.40	2.304	0.004
	0.50	2.328	0.006
	0.60	2.351	0.007
	0.70	2.371	0.010
	0.80	2.377	0.011
Hexene	0.01	2.001	0.026
	0.02	2.060	0.030
	0.02	2.104	0.030
	0.03	2.138	0.030
	0.05	2.245	0.033
	0.08	2.309	0.034
	0.10	2.358	0.035
	0.20	2.462	0.037
	0.30	2.508	0.035
	0.40	2.535	0.039
	0.50	2.556	0.039
	0.60	2.572	0.039
	0.70	2.584	0.038
	0.80	2.583	0.037
Heptane	0.01	1.597	0.004
	0.03	1.694	0.003
	0.05	1.779	0.006
	0.08	1.837	0.005
	0.10	1.879	0.007
	0.20	1.976	0.007
	0.30	2.024	0.005

	0.40	2.054	0.005
	0.50	2.077	0.001
	0.60	2.094	0.001
	0.70	2.110	0.003
	0.80	2.122	0.001
Toluene	0.01	2.617	0.007
	0.02	2.758	0.003
	0.05	2.872	0.003
	0.07	2.939	0.003
	0.10	2.984	0.002
	0.20	3.088	0.002
	0.30	3.155	0.006
	0.40	3.203	0.008
	0.50	3.244	0.006
	0.60	3.284	0.008
	0.70	3.321	0.009
	0.80	3.357	0.017

Table S7. Adsorption isotherms of hydrocarbon gases in ZIF-11 at 308 K (Figure 2B)

Sorbate	Pressure (bar)	Uptake (mmol/g)	Standard Deviation (mmol/g)
Propane	0.041	0.77	0.02
	0.092	0.99	0.03
	0.179	1.34	0.03
	0.276	1.68	0.03
	0.450	2.22	0.06
	0.644	2.61	0.09
	0.846	2.85	0.10
	1.306	3.04	0.19
	1.795	3.16	0.21
	2.248	3.18	0.19
	2.680	3.21	0.24
<i>n</i> -Butane	0.038	1.34	0.08
	0.088	2.24	0.07
	0.178	2.72	0.07
	0.277	2.88	0.06
	0.452	3.00	0.07
	0.646	3.04	0.09
	0.847	3.11	0.04

Table S8. Thermodynamically corrected vapor diffusivities in ZIF-11 at 308 K. Sorbates labeled with crystal sizes used during diffusion experiments (Figures 3 and 4)

Sorbate	Fractional Occupancy (θ)	Diffusivity (cm ² /s)	Error (cm ² /s)
Methanol 36 μ m	0.065	7.8E-10	1.5E-10
	0.235	1.1E-09	3.0E-10
	0.483	1.9E-09	2.1E-10
	0.692	9.4E-10	4.4E-11
	0.808	2.2E-09	1.6E-10
	0.854	3.7E-09	3.7E-10
Ethanol 36 μ m	0.103	2.1E-10	3.6E-12
	0.164	5.6E-10	5.0E-11
	0.699	5.2E-10	2.7E-11
	0.789	6.5E-10	1.0E-10
	0.839	9.7E-10	1.7E-10
	0.894	1.4E-09	5.5E-10
1-Propanol 22 μ m	0.135	5.0E-11	3.4E-12
	0.169	7.7E-11	1.9E-11
	0.414	4.5E-11	1.1E-12
	0.564	6.3E-11	9.1E-12
	0.655	6.1E-11	5.6E-12
	0.729	9.8E-11	3.3E-12
1-Butanol 22 μ m	0.692	7.2E-12	5.3E-13
	0.712	8.2E-12	2.7E-12
	0.774	1.9E-11	1.2E-12
	0.805	2.9E-11	1.7E-12
	0.828	3.4E-11	8.4E-12
	0.887	7.6E-11	3.7E-11
	1.380	1.0E-10	1.8E-11
Propane 36 μ m	0.213	4.9E-08	2.7E-09
	0.277	1.4E-07	1.0E-08
	0.372	7.4E-08	2.5E-08
<i>n</i> -Butane 36 μ m	0.401	8.5E-09	1.9E-09
	0.674	5.5E-09	2.1E-09

	0.816	1.4E-08	8.8E-10
Hexane	0.739	4.0E-11	5.3E-12
22 μm	0.762	3.7E-10	7.6E-12
	0.781	8.5E-10	3.6E-11
	0.795	8.8E-10	1.2E-11
	0.839	3.8E-09	1.1E-10
Hexene	0.775	7.3E-11	1.6E-12
22 μm	0.797	9.1E-11	4.6E-12
	0.814	1.4E-10	7.0E-11
	0.828	1.3E-10	7.3E-11
Heptane	0.753	2.3E-11	6.6E-13
22 μm	0.798	2.8E-11	2.1E-12
	0.838	6.2E-11	8.7E-12
	0.866	8.7E-11	1.7E-11
	0.885	8.5E-11	1.0E-11
	0.931	2.5E-10	6.6E-11

Table S9. Measured libration angles of various ZIFs (Figure 5)

Temperature (K)	ZIF-11 (deg)	ZIF-8 (deg)	ZIF-7 (deg)
173.15	21.8	37.7	21.3
198.15	22.6	38.5	21.5
223.15	23.9	39	21.7
248.15	25	39.3	22
273.15	25.5	39.7	22.2
298.15	25.6	40.1	22.4
323.15	25.7	40.7	22.6
348.15	25.8	41.1	23
373.15	26	41.6	23.4
398.15	26.3	41.9	23.8
423.15	26.9	42.4	24.4

Table S10. Thermodynamically-corrected vapor diffusivities of propane and *n*-butane vs. temperature in ZIF-11 and ZIF-8. ZIF-8 data reproduced from previously published data.⁹ (+/-) represents the standard deviation of measurements (Figure 7).

Temperature (K)	ZIF-11 (cm ² /s)				ZIF-8 (cm ² /s)			
	Propane	+/-	<i>n</i> -Butane	+/-	Propane	+/-	<i>n</i> -Butane	+/-
253	2.2E-08	6.0E-09	-	-	-	-	-	-
273	2.3E-08	1.6E-09	2.6E-09	3.4E-10	5.3E-12	1.0E-12	-	-
293	-	-	-	-	1.6E-11	1.7E-12	2.5E-12	4.3E-13
298	5.0E-08	1.7E-08	5.6E-09	4.0E-10	-	-	-	-
308	5.0E-08	2.7E-09	8.3E-09	1.8E-09	-	-	-	-
313	-	-	-	-	3.6E-11	4.2E-12	5.1E-12	3.0E-13
318	-	-	7.8E-09	1.0E-09	-	-	-	-
333	-	-	-	-	-	-	1.3E-11	1.4E-12

Table S11. Thermodynamically-corrected diffusivity of methane in ZIF-11 (Figure 9).

Temperature (K)	Diffusivity (cm ² /s)	Standard Deviation (cm ² /s)
115	3.3E-11	7.4E-12
125	3.2E-10	9.3E-11
135	3.7E-09	3.3E-09
145	9.6E-09	3.9E-09
155	1.6E-08	1.2E-09
165	3.4E-08	8.7E-09

S7. REFERENCES

1. Crank, J., *The Mathematics of Diffusion*. 2nd ed.; Oxford University Press: Oxford, 1975.
2. Brandani, S., Analysis of the Piezometric Method for the Study of Diffusion in Microporous Solids: Isothermal Case. *Adsorption* **1998**, *4*, 17-24.
3. Kärger, J. R., D. M.; Theodorou, D. N., *Diffusion in Nanoporous Materials*. Wiley-VCH: Weinheim, Germany, 2012.
4. Ruthven, D. M., Sorption Kinetics for Diffusion-Controlled Systems with a Strongly Concentration-Dependent Diffusivity. *Chem. Eng. Sci.* **2004**, *59*, 4531-4545.
5. Do, D. D., *Adsorption Analysis : Equilibria and Kinetics*. Imperial College Press: London, 1998.
6. Spiess, H. W., Molecular Dynamics of Solid Polymers as Revealed by Deuteron Nmr. *Colloid. Polym. Sci.* **1983**, *261*, 193-209.
7. Macho, V.; Brombacher, L.; Spiess, H. W., The Nmr-Weblab: An Internet Approach to Nmr Lineshape Analysis. *Appl. Magn. Reson.* **2001**, *20*, 405-432.
8. Kolokolov, D.; Stepanov, A.; Guillermin, V.; Serre, C.; Frick, B.; Jobic, H., Probing the Dynamics of the Porous Zr Terephthalate UiO-66 Framework Using 2h Nmr and Neutron Scattering. *The Journal of Physical Chemistry C* **2012**, *116*, 12131-12136.
9. Pimentel, B. R.; Lively, R. P., Enabling Kinetic Light Hydrocarbon Separation Via Crystal Size Engineering of Zif-8. *Ind. Eng. Chem. Res.* **2016**, *55*, 12467-12476.